



# One-step hydrothermal synthesis of porous 3D reduced graphene oxide/TiO<sub>2</sub> aerogel for carbamazepine photodegradation in aqueous solution



Mohsin Nawaz, Waheed Miran, Jiseon Jang, Dae Sung Lee\*

Department of Environmental Engineering, Kyungpook National University, 80 Daehak-ro, Buk-gu, Daegu 41566, Republic of Korea

## ARTICLE INFO

### Article history:

Received 3 August 2016  
Received in revised form  
28 September 2016  
Accepted 5 October 2016  
Available online 7 October 2016

### Keywords:

Carbamazepine  
Hydrothermal treatment  
Hydrogel/aerogel  
Titanium dioxide  
Photodegradation

## ABSTRACT

In this study, the three-dimensional (3D) reduced graphene oxide/TiO<sub>2</sub> (RGOT) aerogel was synthesized by a facile one-step hydrothermal treatment, and its photocatalytic efficiency was evaluated in the photodegradation of recalcitrant carbamazepine (CBZ) in aqueous solution. RGOT exhibited high adsorption and an almost two-fold higher photodegradation ability than bare TiO<sub>2</sub> as more than 99% CBZ removal was observed within 90 min in 10 ppm aqueous solution of the latter. The mass ratio of TiO<sub>2</sub> in the RGOT aerogel substantially affected CBZ adsorption and photocatalytic degradation, with the optimal TiO<sub>2</sub>/GO ratio in RGOT found to be 2:1. The chemical bonding between TiO<sub>2</sub> and GO and the effective reduction of the latter during RGOT synthesis were also considered to achieve high photocatalytic efficiency, because the physical mixture of GO and TiO<sub>2</sub> showed a lower photocatalytic CBZ degradation ability than bare TiO<sub>2</sub>. The macroporous 3D structure, abundant surface sites for anchoring the catalyst, effective charge separation, and mass transportation of CBZ near the photocatalyst surface are the attractive features of RGOT aerogels, promoting their use in resolving environmental issues.

© 2016 Elsevier B.V. All rights reserved.

## 1. Introduction

The production and use of pharmaceuticals for improving human and animal health has increased during the last few decades. After their disposal, these pharmaceuticals end up as persistent contaminants in the water systems, having been found in wastewater and surface water at concentrations of ng/L to µg/L [1,2]. Although these compounds are present in very low concentrations, their continuous discharge into the water systems may pose a long-term potential threat for aquatic and terrestrial organisms [3]. The recalcitrant pharmaceutical compound carbamazepine (CBZ), an antiepileptic and psychotropic drug, is one of the most frequently detected pharmaceuticals [4–7] and was proposed as an anthropogenic marker for water systems [8,9]. The high frequency of CBZ detection in water systems is due to its low biodegradation rate and high persistence [7,10,11], since conventional water treatment plants are not designed to deal with recalcitrant pollutants such as CBZ [12]. Under these circumstances, the photodegradation of CBZ using materials based on titanium dioxide (TiO<sub>2</sub>) appears to be a suitable option. TiO<sub>2</sub> is a low-cost, non-toxic, and

highly photostable material, which is most promising for the photocatalytic degradation of recalcitrant pollutants [13,14]. However, the low quantum yield due to the recombination of electron-hole pairs limits its practical application [15]. Various attempts to avoid this recombination have been reported, such as metal-ion or non-metal doping of the crystalline TiO<sub>2</sub>, incorporation of noble metals in the TiO<sub>2</sub> matrix, and composites with carbonaceous materials and other metal oxides [16–21]. Among these species, the incorporation of carbon materials (activated carbon, carbon nanotubes, fullerenes, and graphene) into TiO<sub>2</sub> offers unique advantages, such as chemical inertness and stability in both acidic and basic media [22], retarded recombination of electron-hole pairs [23], and integrated adsorption plus high photocatalytic activity [24]. In particular, graphene has emerged as an extraordinary material due to its excellent charge carrier mobility, large specific surface area, outstanding electrical conductivity, and high thermal/chemical stability [25,26]. In the case of TiO<sub>2</sub>/graphene composites, graphene not only provides support for TiO<sub>2</sub> nanoparticles, but also prevents electron-hole pair recombination by increasing the electron charge transfer rate, which, in turn, accelerates the photodegradation of pollutants [27–30]. However, the deficiency of functional groups on the plane edges of non-functionalized graphene impedes the formation of graphene/TiO<sub>2</sub> composite materials [31]. The reduced graphene oxide (RGO) route is suitable for the synthesis

\* Corresponding author.

E-mail address: [daesung@knu.ac.kr](mailto:daesung@knu.ac.kr) (D.S. Lee).

of RGO-TiO<sub>2</sub> (RGOT) composites due to the excessive availability of functional groups in the basal plane as well as on the plane edges of GO to bond with TiO<sub>2</sub> [31,32]. Moreover, the reduction of GO also helps to recover the deteriorated electronic properties owing to the functional groups available on GO and the resulting excellent mobility of charge carriers [33].

Recently, the synthesis of three-dimensional (3D) hydrogel/aerogel RGOT structures with high photocatalytic activity using hydrothermal treatment have been reported by various researchers [34–37]. In most of the previous studies, *in-situ* (using a precursor for TiO<sub>2</sub> nanoparticle formation) and, in some cases, *ex-situ* (direct use of TiO<sub>2</sub> nanoparticles) techniques were used above 100 °C to synthesize RGOT composites. Almost all researchers used dyes to evaluate the efficiency of the composite material.

In the current study, both *in-situ* and *ex-situ* techniques were applied using a facile one-step hydrothermal process below 100 °C, but the RGOT hydrogel/aerogel was only successfully synthesized in the *ex-situ* case. Contrary to previous researchers, we used the RGOT aerogel as a superior photocatalyst to degrade CBZ, which is a more recalcitrant emerging micropollutant than dyes. The macroporous 3D structure, larger support for the settlement of TiO<sub>2</sub> nanoparticles (as compared to the 2D structure), and mass transportation of CBZ close to the photocatalyst are the RGOT features that make it an efficient photocatalytic system compared to bare TiO<sub>2</sub> nanoparticles.

## 2. Experimental section

### 2.1. Materials

Carbamazepine, TiO<sub>2</sub> (anatase; purity 99.7%, BET specific surface area 50 m<sup>2</sup>/g, average crystal size < 25 nm), and L-ascorbic acid were purchased from Sigma-Aldrich (South Korea). NaNO<sub>3</sub>, H<sub>2</sub>SO<sub>4</sub>, and H<sub>2</sub>O<sub>2</sub> were sourced from Duksan (South Korea). KMnO<sub>4</sub> was obtained from Junsei Chemicals (South Korea), and natural flake graphite powder and Ti(SO<sub>4</sub>)<sub>2</sub> were purchased from Kanto (Japan). All reagents were of analytical grade and were used without further purification.

### 2.2. Synthesis of GO

GO was prepared using the modified Hummers' method [38,39]. In brief, natural flake graphite powder (1 g) and NaNO<sub>3</sub> (1 g) were added to H<sub>2</sub>SO<sub>4</sub> (46 mL) under stirring, while the temperature was kept at 0 °C using an ice bath. KMnO<sub>4</sub> (6 g) was very slowly added under the same conditions. The flask was subsequently transferred into an oil bath at 35 °C and stirred for two days. The solution was subsequently diluted with distilled water to twice the volume of H<sub>2</sub>SO<sub>4</sub>, and the reaction was finally completed by adding 30% H<sub>2</sub>O<sub>2</sub> until the gas evolution stopped. Repetitive washing of the solution with distilled water was performed at 15000 rpm until the solution pH became equal to 5. The acquired solid GO was dried in a vacuum oven at 30 °C.

### 2.3. Synthesis of RGOT 3D aerogel

TiO<sub>2</sub> nanoparticles in different mass ratios with respect to GO (1:1 to 4:1) were added under sonication to homogeneous aqueous GO dispersions (4 mg/mL, 10 mL) in a 20-mL glass vial. A certain amount of L-ascorbic acid was added under magnetic stirring and the sealed glass vial was kept at 95 °C for 1 h in an oil bath. The obtained hydrogel was washed with DI water several times and finally freeze-dried for characterization and further use in photocatalytic studies. The synthesized RGO and RGOT (1:1 to 4:1) hydrogels and aerogels are shown in Fig. S1. The *in-situ* synthesis of

the RGO-TiO<sub>2</sub> composite was attempted using Ti(SO<sub>4</sub>)<sub>2</sub> as a precursor. Moreover, lab-made TiO<sub>2</sub> nanoparticles were obtained using the method of Qiu et al. [36] and their photocatalytic activity in CBZ degradation was checked and compared with that of commercial TiO<sub>2</sub>.

### 2.4. Characterization

X-ray diffraction (XRD) data were collected using an X'pert APD X-ray diffractometer (Philips, Netherlands) with Cu K<sub>α</sub> radiation and a scanning range of 5–80°. A Perkin-Elmer spectrum one Fourier transform infrared (FT-IR) spectrometer (Frontier, USA) was used to record FT-IR spectra in the range of 4000–400 cm<sup>−1</sup>. Raman spectra were recorded using an inVia reflex Raman spectrophotometer (Renishaw, UK). The BET specific surface areas were measured by the nitrogen adsorption-desorption method using Autosorb-iQ and Quadrasorb SI instruments (Quantachrome, USA). X-Ray photoelectron spectroscopy (XPS) was obtained using a Quantera SXM (ULVAC-PHI, Japan) to study the surface composition of RGOT samples by recording Ti2p, C1s and O1s XPS spectra. Thermogravimetric analysis (TGA) was conducted by using SDT Q600 (TA Instruments, Japan) apparatus at a heating rate of 10 °C/min in the temperature range of 25–800 °C under a dynamic atmosphere of nitrogen. The ultraviolet–visible (UV–vis) diffuse reflectance absorption spectra of the prepared samples were obtained by using a (8453, Agilent, USA) spectrophotometer. The morphology and uniform anchoring of TiO<sub>2</sub> on RGO in RGOT were analyzed using field emission scanning electron microscopy (FE-SEM; S-4800, Hitachi, Japan) and transmission electron microscopy (FE-TEM; FEI, Titan G2 ChemiSTEM Cs Probe, Netherlands), respectively. The pictorial images were taken using a digital camera (E3700, Nikon, Japan).

### 2.5. Adsorption-desorption equilibrium study

The adsorption-desorption equilibrium was established by introducing 0.5 g L<sup>−1</sup> (each) of TiO<sub>2</sub>, GO-TiO<sub>2</sub> physical mixture, and RGOT (1:1–1:4) into an aqueous CBZ solution (10 ppm, 200 mL) in the dark 40 min prior to the photocatalytic process. Samples were drawn every 10 min until equilibrium was reached, filtered through a 0.22 μm syringe filter, and analyzed using a UV–vis spectrophotometer to determine the residual concentration of CBZ at λ = 285 nm. The adsorption capacity (*q*, mg/g) was calculated by using Eq. (1):

$$q = \frac{(C_0 - C_t)V}{m} \quad (1)$$

where *C*<sub>0</sub> and *C*<sub>t</sub> are the initial and final concentrations of the CBZ solution, respectively, *V* is the CBZ solution volume (L), and *m* is the mass (g) of TiO<sub>2</sub>, GO-TiO<sub>2</sub>, and/or RGOT.

### 2.6. Photocatalytic activity and photoelectrochemical measurements

The photocatalytic activities of TiO<sub>2</sub> (commercial and lab-made), GO-TiO<sub>2</sub> (physical mixture), and RGOT aerogels (1:1–1:4) were separately evaluated by the photocatalytic degradation of CBZ in aqueous solution under UV light. In all cases, 0.5 g L<sup>−1</sup> of each photocatalyst was individually dispersed in 10 ppm CBZ aqueous solution. Even though the concentration of CBZ was much higher than the representative values in water and/or wastewater, it did not affect the process kinetics, reaction mechanism, and the transformation products [40]. The suspensions were placed in the dark under stirring for 40 min to establish the adsorption-desorption equilibrium between the photocatalyst and CBZ prior to irradiation. The photodegradation of CBZ was then carried out in an

immersion well photoreactor, with the setup details reported in our previous study [41]. The UV irradiation intensity hitting the CBZ solution in the reactor was measured with a BLACK-comet concave grating spectrometer (StellarNet Inc., USA) and was found to be  $13.5 \pm 1 \text{ W m}^{-2}$  in the range of 300–400 nm, with the peak wavelength at 365 nm. At given intervals, samples were extracted and filtered through a 22  $\mu\text{m}$  syringe filter to separate the photocatalysts from the supernatant prior to the analysis.

Photoelectrochemical measurements, Linear Sweep Voltammetry (LSV), were performed using the standard three-electrode setup. The RGOT film was used as the working electrode, saturated calomel electrode (SCE) was the reference electrode, and a platinum wire was the counter electrode. Working electrode was prepared by mixing RGOT (20 mg) with 5 wt% nafion solution (0.2 mL) to make a slurry and the slurry was coated on the fluorine–tin oxide (FTO) glass by the doctor blade method.  $\text{Na}_2\text{SO}_4$  (0.1 M) aqueous solution was used as the electrolyte. Subsequently the photocurrent was measured in the dark and under the illumination of light.

### 2.7. Determination of residual CBZ

The residual CBZ concentration in aqueous samples was first analyzed using UV–vis spectrophotometry (8453, Agilent, USA) to measure the intensity change of the maximum absorbance peak at 285 nm and was then confirmed by high performance liquid chromatography (HPLC, Shimadzu LC20AD). The HPLC instrument was equipped with a Zorbax Eclipse XDB-C18 column (150 mm  $\times$  4.6 mm, 5  $\mu\text{m}$ ), and a UV/vis detector (SPD-20A) was used in isocratic mode to analyze the concentration of CBZ. A methanol/water (with 1% acetic acid) mixture (60:40, v/v) was used as the mobile phase, with a flow rate of  $0.6 \text{ mL min}^{-1}$ . The detection wavelength was  $\lambda = 285 \text{ nm}$ . Degradation products were detected by liquid chromatography–tandem mass spectrometry (LC–MS/MS) using LC (1200 HPLC system)–MS (6410 QqQ, Agilent, USA). The results of CBZ photodegradation obtained by HPLC were compared with the ones obtained by UV–vis spectrophotometry and are shown in Fig. S2. No large difference in the results obtained by both instruments was detected.

## 3. Results and discussion

It is well known that both GO and  $\text{TiO}_2$  have a hydrophilic nature. Once  $\text{TiO}_2$  nanoparticles and GO were co-dispersed in water, the color of  $\text{TiO}_2$  changed from white to light brown, indicating strong coupling to GO. When this suspension was kept without stirring for 5 min, the cotton-like structure of GO– $\text{TiO}_2$  suspension was formed, leaving the residual solution clear and colorless, which indicated that the interaction between  $\text{TiO}_2$  and GO was much stronger than between  $\text{TiO}_2$  and water molecules [33].

The distribution of oxygenated functional groups on GO strengthened its interaction with  $\text{TiO}_2$  nanoparticles. Mixing of L-ascorbic acid to the GO– $\text{TiO}_2$  suspension under stirring resulted in a homogeneous solution, which was finally converted into the RGOT hydrogel after the hydrothermal treatment under stationary conditions at  $95^\circ\text{C}$ . The successful reduction of GO to RGO, i.e., the formation of 3D RGOT hydrogel, was confirmed by the change in color from brownish-yellow to greyish-black. We carried out both *in-situ* and *ex-situ* syntheses of RGOT in presence of  $\text{Ti}(\text{SO}_4)_2$  and  $\text{TiO}_2$  nanoparticles, respectively, and it was observed that the hydrogel was only formed in the latter case, while two separated phases were generated in the former case (Fig. S3) due to less or no coupling of *in-situ* grown  $\text{TiO}_2$  with GO. Therefore, the initial strong coupling between  $\text{TiO}_2$  nanoparticles and GO prior to the hydrothermal process and the successive reduction of GO to RGO during hydrothermal treatment was the key factor for the

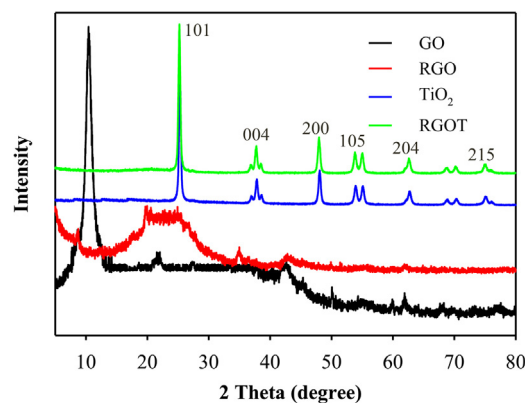


Fig. 1. X-ray diffraction pattern of GO, RGO,  $\text{TiO}_2$ , and RGOT.

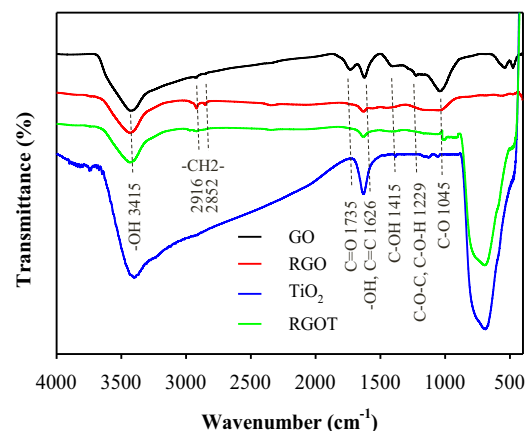


Fig. 2. FT-IR spectra of GO, RGO,  $\text{TiO}_2$ , and RGOT.

formation of the RGOT hydrogel [33]. The successful formation of the latter was confirmed by different characterization techniques, including XRD, FT-IR, Raman spectroscopy, XPS, TGA, UV–vis, SEM–EDS, and TEM.

### 3.1. Characterization of GO and RGOT aerogel

The XRD patterns of GO, RGO,  $\text{TiO}_2$ , and RGOT are shown in Fig. 1, which makes it clear that the diffraction peak of GO at  $2\theta = 11^\circ$  disappeared, and a new wide diffraction peak of RGO appeared after the hydrothermal process. The appearance of a new peak confirmed the elimination of oxygenated functional groups from RGO and also proved the existence of strong  $\pi$ – $\pi$  stacking interactions between the RGO sheets as the major cause of gelation [42]. The similarity in the XRD patterns of  $\text{TiO}_2$  and the RGOT aerogel was due to the limited amount and relatively low diffraction intensity of RGO in the latter [34,35]. XRD analysis of the *in-situ* synthesized RGO– $\text{TiO}_2$  composite was also carried out. Therein (Fig. S4), the rutile  $\text{TiO}_2$  phase was observed alongside with the anatase phase, while in the *ex-situ* case, the pure anatase form was used.

The reduction degree of GO in RGO and RGOT aerogels was investigated by FT-IR spectroscopy (Fig. 2). The FT-IR spectrum of GO demonstrates the presence of numerous oxygenated functional groups with absorption peaks at  $1045 \text{ cm}^{-1}$  (epoxy or alkoxy C–O),  $1229 \text{ cm}^{-1}$  (epoxide C–O–C or phenolic C–O–H stretch),  $1415 \text{ cm}^{-1}$  (alcoholic C–OH bend),  $1626 \text{ cm}^{-1}$  (water –OH bend and C=C stretch),  $1735 \text{ cm}^{-1}$  (carboxylate or ketone C=O stretch), and  $3415 \text{ cm}^{-1}$  (water–OH stretch) [33,35].

The disappearance or substantial intensity decrease of the oxygenated functional groups after the hydrothermal treatment of

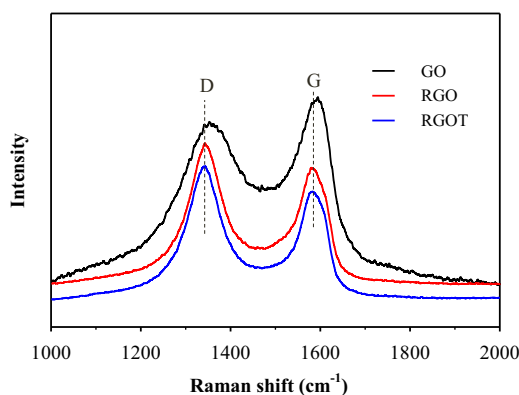


**Fig. 3.** Raman spectra showing the characteristic D and G bands of GO, RGO, and RGOT.

GO further confirmed the reduction of the latter to RGO. In the case of TiO<sub>2</sub> nanoparticles, the wide peak in the 400–900 cm<sup>-1</sup> range corresponded to the vibration of the Ti–O–Ti bond, and absorption peaks at 3415 cm<sup>-1</sup> and ca. 1626 cm<sup>-1</sup> were due to the water hydroxyl group [43]. In the case of the RGOT aerogel, the oxygenated functional groups demonstrated low absorption peak intensity in the range of 1000–2000 cm<sup>-1</sup>. However, the strong peaks in the range of 400–1000 cm<sup>-1</sup> could be attributed to a combination of the Ti–O–Ti and Ti–O–C stretching vibrations. The existence of Ti–O–C bonds in the RGOT aerogel implies chemical bonding between TiO<sub>2</sub> and RGO [27]. The FT-IR spectra of the *in-situ* synthesized RGO–TiO<sub>2</sub> composite are shown in Fig. S5. Although the number of oxygenated functional groups decreased, confirming the reduction of GO, the exact reason behind the unsuccessful hydrogel structure formation is not known. It may be due to the lesser interaction of GO and the *in-situ* synthesized TiO<sub>2</sub> nanoparticles.

More evidence on the reduction of GO to RGO and the formation of RGOT aerogel can be obtained by Raman spectroscopy. Fig. 3 shows the Raman spectra of GO, RGO, and RGOT, with the D band

(A<sub>1g</sub> breathing mode) and the G band (E<sub>2g</sub> in-plane vibrational mode) present in all spectra. The D band corresponds to disordered carbon due to structural defects, whereas the G bands represents tangential C–C stretching vibrations [44]. The intensity ratio of these bands,  $I_D/I_G$ , is a characterization tool for short-ranged sp<sup>2</sup> carbon moieties and sp<sup>3</sup>-hybridized carbon atoms in RGO to evaluate the extent of defects/disorder in graphitic structures [44,45]. High  $I_D/I_G$  values are attributed to an increased number of sp<sup>3</sup> defects/disorder, implying a decrease in the average size of the sp<sup>2</sup> carbon moieties, and hence an increased degree of GO reduction [46,47]. The  $I_D/I_G$  values for RGO and RGOT are 1.28 and 1.41, respectively, much higher than the  $I_D/I_G$  value of 0.78 for GO. This confirms that the hydrothermal process leads to a large number of sp<sup>3</sup> defects in RGO and RGOT during the successful reduction of GO. The highest  $I_D/I_G$  value in case of RGOT further confirmed the strong chemical bonding between TiO<sub>2</sub> nanoparticles and RGO nanosheets, as the existence of Ti–O–C bonds was previously confirmed by FT-IR analysis. Moreover, the shifting of the GO-assigned D band from 1353 cm<sup>-1</sup> to ca. 1341 cm<sup>-1</sup> and the G band from 1594 cm<sup>-1</sup> to 1588 cm<sup>-1</sup> in the case of RGOT is another confirmation of successful GO reduction [48].

The BET surface area of RGO, measured by the nitrogen adsorption-desorption method, was 209 m<sup>2</sup>/g (Fig. 4(a) and (b)), but the surface area decreased with the inclusion of different ratios of TiO<sub>2</sub> nanoparticles in the RGOT aerogel. In the case of RGOT (1:4), the BET surface area was only 65 m<sup>2</sup>/g, as shown in Fig. 4(c) and (d), slightly higher than that of bare TiO<sub>2</sub> (Fig. S6). The change in RGOT BET surface area can be attributed to the uniform dispersion of TiO<sub>2</sub> with ample coverage of RGO nanosheets as the surface area changed with the increase of TiO<sub>2</sub> concentration while the RGO concentration was kept constant. The surface wettability of the RGOT aerogel also varied from hydrophobic to hydrophilic in the following order: RGOT (1:1) > RGOT (1:2) > RGOT (1:3) > RGOT (1:4). The abovementioned surface wettability is an important factor, since the aerogel is used for the degradation of miscible and immiscible pollutants [37]. Moreover, the photodegradation of CBZ in this study was also affected by changes in TiO<sub>2</sub> concentration, as is dis-

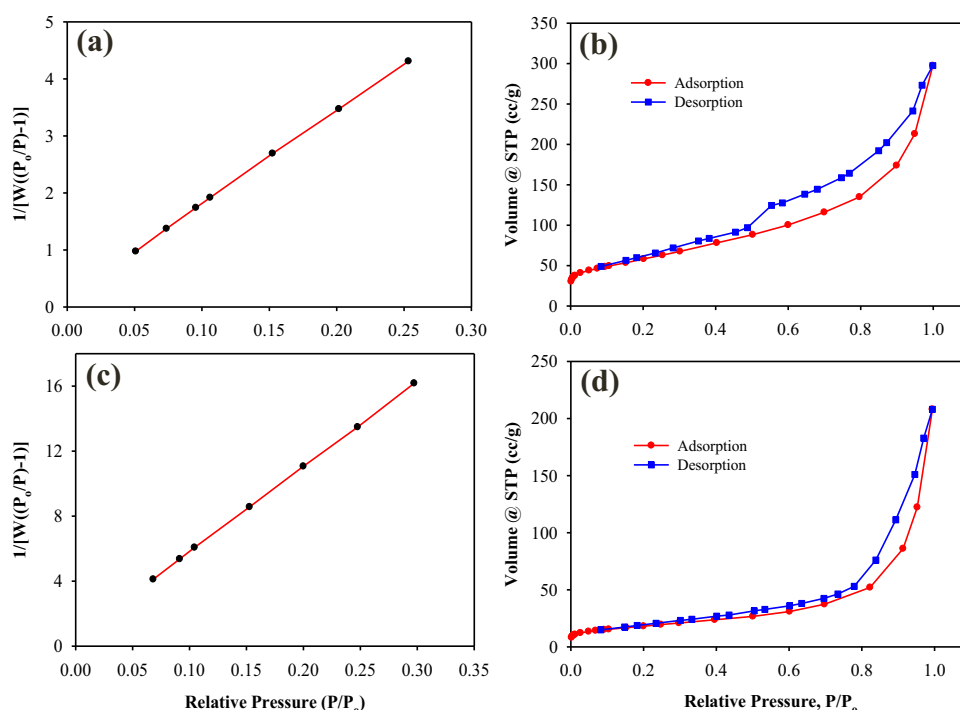


**Fig. 4.** BET surface area analysis: (a) RGO isotherm linear plot, (b) RGO surface area plot, (c) RGOT (1:4) isotherm plot, and (d) RGOT (1:4) surface area plot.



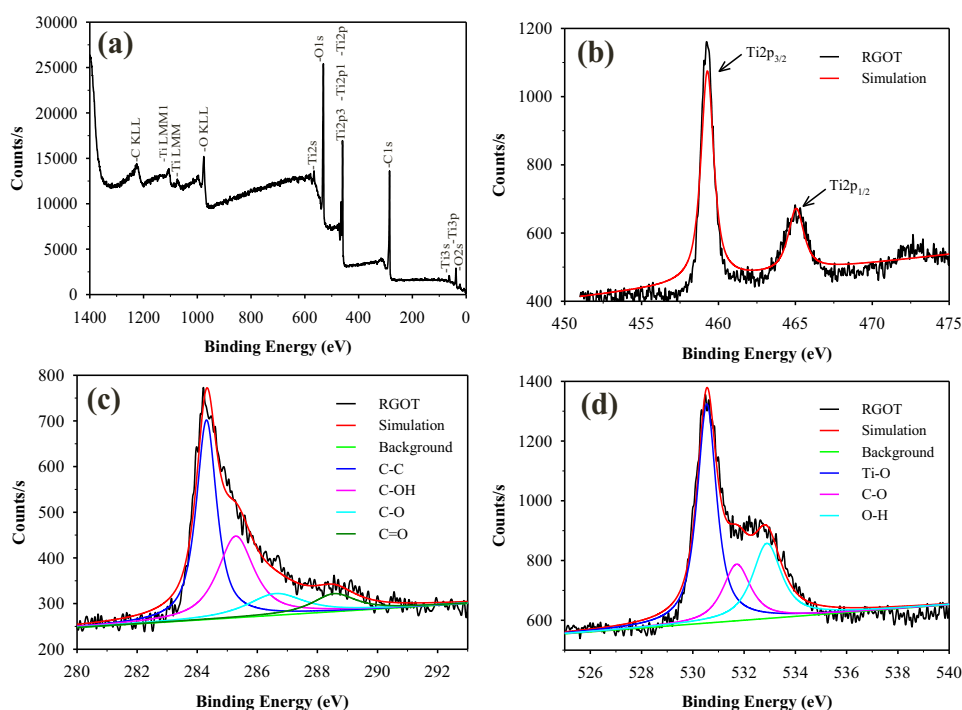


Fig. 5. XPS spectra of RGOT (a) wide scan, (b) the deconvolution of Ti2p, (c) C1s, (d) O1s.

cussed later (Photocatalytic Activity and Kinetics of RGOT). Even though the surface areas of bare  $\text{TiO}_2$  and RGOT (1:4) were almost similar, the higher adsorption and photocatalytic degradation of CBZ can be credited to the 3D porous structure of RGOT [34].

The XPS analysis was performed to further study the surface state of RGOT (Fig. 5). The wide scan XPS spectra (Fig. 5(a)) show the existence of C, O, and Ti in RGOT aerogel. Two peaks centered at 459.4 and 465.1 eV, with a peak separation of 5.7 eV, assigned to  $\text{Ti } 2p_{3/2}$  and  $\text{Ti } 2p_{1/2}$ , respectively, (Fig. 5(b)) implies the presence of the  $\text{Ti}^{4+}$  in pure anatase phase [49]. Fig. 5(c) shows the corresponding high resolution XPS and curve fitting of the C1s peaks. The energies at 284.4, 285.3, 286.6 and 288.6 eV can be assigned to C–C, C–OH, C–O and C=O, respectively [50]. These oxygen-containing functional groups examined by XPS are in good agreement with the studies of FTIR. The O1s spectra displayed in Fig. 5(d) is fitted with three peaks. The peaks around 530.5 eV (Ti–O bond) and 532.9 eV (O–H bond) can be ascribed to the bulk  $\text{O}^{2-}$  from  $\text{TiO}_2$  and –OH adsorbed on the surface of RGOT aerogel, while the peaks at 531.7 eV can be ascribed to C–O bond [51]. The acquired results demonstrates the good chemical linkage between  $\text{TiO}_2$  and RGO and can facilitate the fast electron transport throughout the graphene network and between the RGO and the anchored  $\text{TiO}_2$  nanoparticles.

Thermal stability of the prepared samples was analyzed by TGA and the curves are shown in Fig. 6. The TGA curve of pure  $\text{TiO}_2$  shows only 3% weight loss up to 800 °C, which may correspond to the loss of adsorbed water. GO has a drastic weight loss starting from 100 °C due to the removal of liable oxygen-containing functional groups and above 550 °C, the  $\text{sp}^2$  hybridized carbon networks in GO and RGO are almost completely degraded [52]. Compared to GO and RGO, the RGOT shows almost 18% weight loss up to 800 °C, which indicates the enhanced thermal stability of RGOT by means of chemical bonding. According to the results analyzed by TGA, it can be anticipated that the RGOT contains 85 wt% and 15 wt% of  $\text{TiO}_2$  and RGO, respectively.

From the UV–vis absorption spectroscopy measurements of the prepared samples (Fig. S7), a distinctive absorption in the UV light

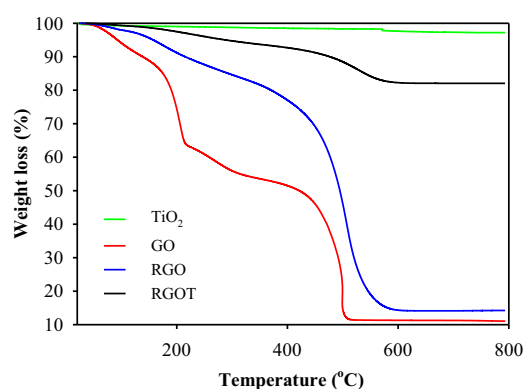


Fig. 6. TGA curves of  $\text{TiO}_2$ , GO, RGO, and RGOT.

range with an edge around 400 nm can be seen in case of  $\text{TiO}_2$  whereas, the inclusion of RGO, GO specific peak around 227 nm disappeared, increased the absorbance in the visible light range for RGOT. This may be due to the absorption contribution of RGO, the enhancement in surface electric charge of  $\text{TiO}_2$ , and the partial restoration of the pi-conjugation network as a result of the hydrothermal and chemical reduction process [53].

### 3.2. Morphology of GO and RGOT aerogel

Fig. 7(a–d) shows FE-SEM images of GO, RGO, RGOT and the result of RGOT aerogel EDX analysis. As can be seen in Fig. 7(b), interconnected 3D crumpled macroporous RGO sheets are obtained after the hydrothermal treatment of GO. Fig. 7(c) shows that the  $\text{TiO}_2$  nanoparticles are uniformly anchored and tightly attached on the outer and inner walls of the porous RGO nanosheets due to a strong interaction between  $\text{TiO}_2$  and RGO. The high-magnification SEM image of RGOT is shown in Fig. S8, where the  $\text{TiO}_2$  nanoparticles and RGO nanosheets are clearly marked. Williams et al. previously reported that  $\text{TiO}_2$  nanoparticles could anchor on RGO nanosheets via physisorption, electrostatic binding, and/or charge

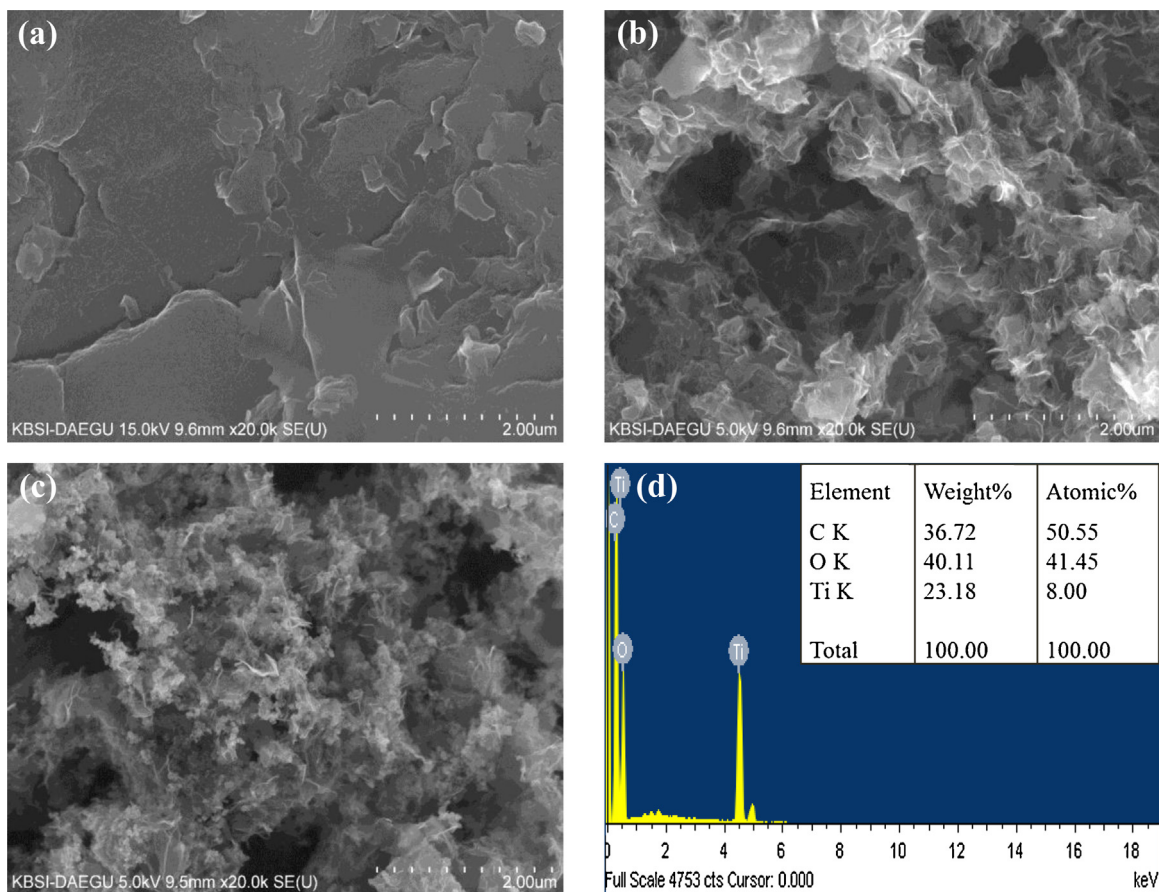


Fig. 7. FE-SEM images: (a) GO, (b) RGO, (c) RGOT; d) EDX analysis of RGOT.

transfer interactions [54]. The observed highly aggregated clusters of the *in-situ* synthesized  $\text{TiO}_2$ , possibly due to the ineffective attachment to RGO, are shown in Fig. S9(a).

The composition of the RGOT aerogel was further analyzed by EDX. Large peaks of titanium, carbon and oxygen were found, showing absence of impurities in the RGOT composite, whereas a high concentration of sulfur was observed for the *in-situ* formed RGO- $\text{TiO}_2$  composite, as shown in Fig. S9(b). The high concentration of sulfur may be another reason for the unsuccessful hydrogel structure formation. Moreover, the lab-made  $\text{TiO}_2$  nanoparticles were separately analyzed by SEM, which detected large aggregates of  $\text{TiO}_2$  nanoparticles, depicted in Fig. S10(a). Interestingly, repetitive washing of  $\text{TiO}_2$  nanoparticles greatly reduced the concentration of sulfur, as shown by EDX analysis (Fig. S10(b)). The small aggregated pores of lab-made  $\text{TiO}_2$  nanoparticles restricted their effective coupling with GO, which resulted in separated layers of RGO nanosheets and  $\text{TiO}_2$  after hydrothermal treatment, as shown in Fig. S3.

Fig. 8(a) and (b) shows the TEM images of the crumpled structure of RGO and the  $\text{TiO}_2$  nanoparticles uniformly anchored on RGO nanosheets in the RGOT aerogel, respectively. The higher loading of  $\text{TiO}_2$  in the RGOT aerogel can be seen in Fig. 8(b). The high-resolution TEM image in the inset of Fig. 8(b) shows a crystalline  $\text{TiO}_2$  nanoparticle with a lattice interspacing of 0.35 nm, similar to that of anatase (101) planes [55]. Fig. 8(c) shows HAADF-STEM image of RGOT. The elemental maps in Fig. 8(d–f) reveal that the distribution of C element is consistent with the profile of RGO sheets, and Ti element along with O element is overlapped as  $\text{TiO}_2$  nanocrystals validating the uniform anchoring of  $\text{TiO}_2$  on RGO nanosheets. The overlapping of C, O and Ti elements in Fig. 8(g) fur-

ther indicates the void dissociation of  $\text{TiO}_2$  nanoparticles from the RGO nanosheets.

### 3.3. Adsorption equilibrium and kinetic studies

The adsorption ability of  $\text{TiO}_2$ , GO- $\text{TiO}_2$  physical mixture, and RGOT aerogels (1:1–1:4) was assessed in lieu of adsorption-desorption equilibrium prior to the photodegradation process. The adsorption ability was greatly enhanced in the case of chemically bonded RGOT aerogel. More than 55% CBZ was adsorbed in case of RGOT (1:1); however, a decrease in adsorption was noticed at an increased amount of  $\text{TiO}_2$  [56]. The amount of adsorbed CBZ in the case of RGOT (1:4) was almost similar to that of  $\text{TiO}_2$ . In order to investigate the mechanism of adsorption, pseudo-first-order and pseudo-second-order kinetic models were applied by using Eqs. (2) and (3).

$$\ln(q_e - q_t) = \ln q_e - k_1 t \quad (2)$$

$$\frac{t}{q_t} = \frac{1}{k_2 q_e^2} + \frac{t}{q_e} \quad (3)$$

where  $q_e$  and  $q_t$  are the amounts of CBZ adsorbed per unit mass at equilibrium and at any time  $t$ , respectively,  $k_1$  ( $\text{min}^{-1}$ ) is the pseudo-first-order adsorption rate coefficient, and  $k_2$  ( $\text{g mg}^{-1} \text{min}^{-1}$ ) is the pseudo-second-order rate coefficient. In this study, the pseudo-second-order rate equation tailored well with the experimental data for CBZ adsorption. As shown in Table 1 under the adsorption section, the values of  $q_{e(\text{cal.})}$  are in close agreement with experimental values  $q_{e(\text{exp.})}$  along with the satisfactory linear regression coefficient ( $R^2$ ) values. Adsorption of the pollutant on or close to the photocatalyst is considered an important

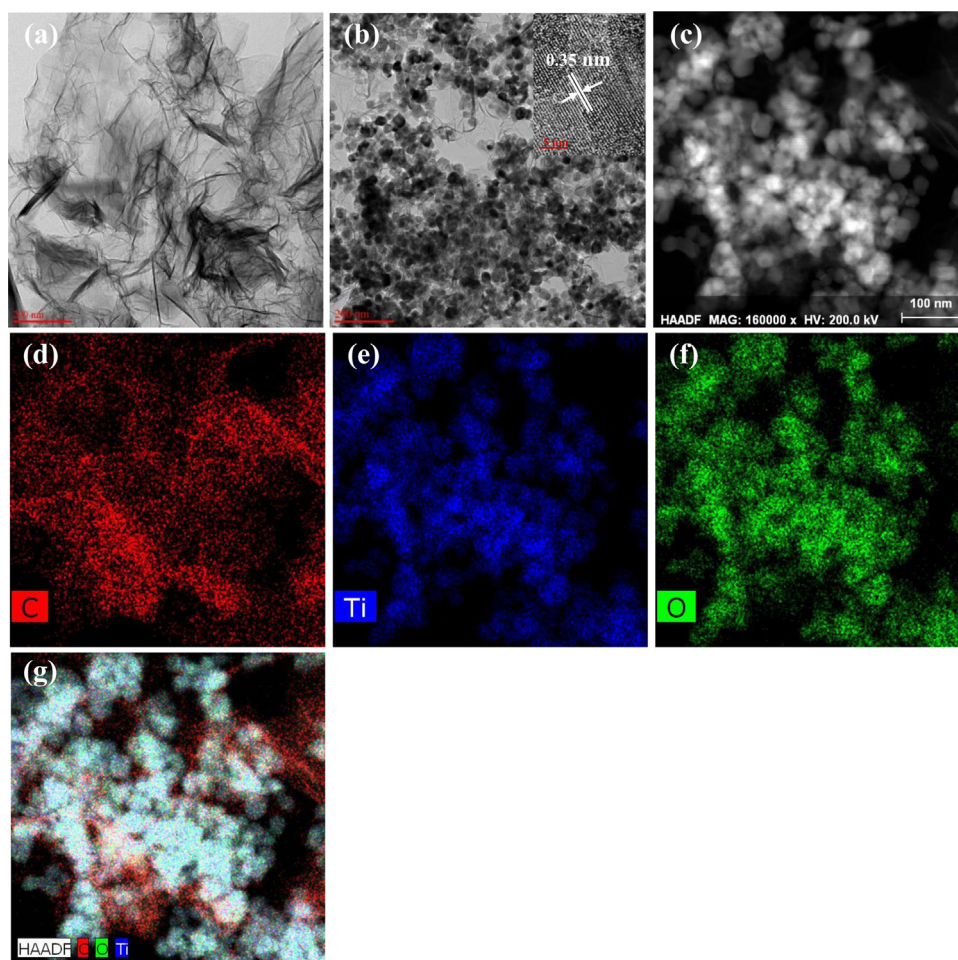


**Fig. 8.** FE-TEM images: (a) RGO, (b) RGOT (inset high-resolution TEM image), (c) HAADF-STEM RGOT image, (d–f) elemental maps of RGOT, (g) overlapping of C, O, and Ti elements.

**Table 1**

Pseudo-second-order reaction rate constant (for adsorption) and  $k_{app}$  values (for photodegradation) using  $\text{TiO}_2$ ,  $\text{GO-TiO}_2$  (physical mixture), and RGOT aerogels (1:1–1:4).

Combination details	Adsorption				Photodegradation		
	$q_{e(\text{exp.})}$ (mg/g)	$q_{e(\text{cal.})}$ (mg/g)	$k_2$	$R^2$	$k_{app}$ ( $\text{min}^{-1}$ )	$R^2$	$t_{1/2}$ (min)
$\text{TiO}_2$	3.37	3.68	0.048	0.925	0.0067	0.864	103.4
$\text{GO-TiO}_2$	0.64	0.66	0.177	0.827	0.0037	0.828	187.3
$\text{RGO-TiO}_2$ (1:1)	11.28	12.48	0.016	0.921	0.0453	0.951	15.3
$\text{RGO-TiO}_2$ (1:2)	6.99	7.64	0.025	0.930	0.0473	0.955	14.7
$\text{RGO-TiO}_2$ (1:3)	5.34	5.83	0.033	0.932	0.0404	0.975	17.2
$\text{RGO-TiO}_2$ (1:4)	3.59	3.86	0.059	0.949	0.0265	0.983	26.2

factor for the effective photodegradation of the former [57,58]. The successful photodegradation of CBZ by the RGOT aerogel may be linked to the rapid adsorption of the former on the RGO surface via  $\pi$ - $\pi$  conjugation followed by diffusion to the  $\text{TiO}_2$  surface [59].

### 3.4. Photocatalytic and photoelectrochemical properties of RGOT

The direct photolysis of CBZ aqueous solution by UV light in absence of catalyst and photocatalytic degradation in presence of  $\text{TiO}_2$  (commercial and lab-made),  $\text{GO-TiO}_2$  physical mixture, and RGOT (1:1–1:4) were investigated (Fig. 9). The direct photolysis of CBZ demonstrated almost negligible degradation of the latter, whereas the photocatalytic degradation reached almost 51% and 31% in the case of commercial and lab-made  $\text{TiO}_2$  nanoparticles, respectively. The change in absorbance, i.e., the photocatalytic degradation of CBZ by lab-made  $\text{TiO}_2$  is shown in Fig. S11. The low

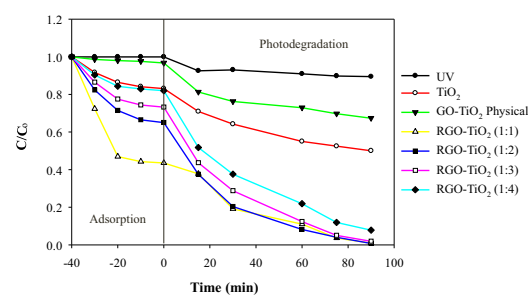


**Fig. 9.** Plot of  $C/C_0$  for the photolysis of CBZ in absence of catalyst and adsorption plus photodegradation of CBZ using  $\text{TiO}_2$ ,  $\text{GO-TiO}_2$  physical mixture, and RGOT aerogel (1:1–1:4).

photocatalytic degradation ability of lab-made  $\text{TiO}_2$  may be due



to the aggregation of nanoparticles, which makes a large portion of  $\text{TiO}_2$  unavailable for the photocatalytic process [60]. After the chemical coupling of  $\text{TiO}_2$  with RGO, the photocatalytic degradation of CBZ was significantly enhanced, achieving almost complete CBZ removal from solution. The photocatalytic activity of the above-mentioned photocatalysts was described using the simplified form of the Langmuir–Hinshelwood (L–H) kinetic model (Eq. (4)), i.e., a pseudo-first-order kinetic equation:

$$\ln \frac{C_t}{C_0} = -k_{\text{app}} t \quad (4)$$

where  $C_0$  and  $C_t$  are the initial and final concentrations of the CBZ solution, respectively,  $k_{\text{app}}$  is the pseudo-first-order rate constant ( $\text{min}^{-1}$ ), and  $t$  is the time (min). The  $k_{\text{app}}$  values were calculated from the slope of the  $\ln C_t/C_0$  versus  $t$  plot for each photocatalyst individually and are reported in Table 1.

Enhanced CBZ photodegradation was observed at a lower  $\text{TiO}_2$  concentration in RGOT, i.e., for RGOT (1:1–1:2), as opposed to RGOT (1:3–1:4). Although the amount of adsorbed CBZ in case of RGOT (1:1) (57%) was much higher than in case of RGOT (1:2) (36%), the photodegradation rate in the former case ( $k_{\text{app}} = 0.0453 \text{ min}^{-1}$ ) was slightly less than in the latter ( $k_{\text{app}} = 0.0473 \text{ min}^{-1}$ ), as shown in Table 1. The small  $k_{\text{app}}$  value for RGOT (1:1) may be due to the dominance of RGO, which provides a large total composite area for high CBZ adsorption but reduces the effective surface area due to the lesser availability of  $\text{TiO}_2$  for the reaction [61].

Moreover, the blockage of UV light flux to the  $\text{TiO}_2$  surface by excessive RGO may be another reason for the lesser  $k_{\text{app}}$  value of RGOT (1:1), as compared with RGOT (1:2) [51]. Zhao et al. reported that the coverage of photocatalyst with superfluous RGO, detrimental for photon absorption, shielded the photocatalyst from absorbing the UV light [62]. The excessive RGO can also promote the recombination of photogenerated charges by acting as a kind of charge carrier recombination center [63]. On the other hand, increasing the concentration of  $\text{TiO}_2$  nanoparticles beyond RGOT (1:2), i.e., RGOT (1:3–1:4), also negatively affected the adsorption and photodegradation. This indicates that an optimum concentration of  $\text{TiO}_2$  must be used to synthesize RGOT and obtain maximum photodegradation of the pollutant. In this study, the optimum concentration of  $\text{TiO}_2$  was twice the amount of GO, i.e., RGOT (1:2), with the higher degradation rates attributed to the uniform anchoring of  $\text{TiO}_2$  on RGO nanosheets. The RGO support aided charge separation by acting as an electron sink and facilitated electron transfer to produce more radicals [64]. Although a negative effect on the adsorption and photodegradation of CBZ was observed in the case of RGOT (1:3–1:4), the  $k_{\text{app}}$  values ( $k_{\text{app}} = 0.0404$  and  $0.0265 \text{ min}^{-1}$  for RGOT 1:3 and RGOT 1:4, respectively) were still higher compared to bare  $\text{TiO}_2$  ( $k_{\text{app}} = 0.0067 \text{ min}^{-1}$ ). This confirms the synergistic effect of the composite of chemically bonded RGO and  $\text{TiO}_2$ , since the efficiency of physically mixed GO and  $\text{TiO}_2$  ( $k_{\text{app}} = 0.0037 \text{ min}^{-1}$ ) was even lower than that of bare  $\text{TiO}_2$ . The negative effect observed for high  $\text{TiO}_2$  concentration may be linked to its aggregation, which restricts the contact between RGO and  $\text{TiO}_2$ , with the lack of synergistic effect ultimately reducing the efficiency of the photocatalytic process [61]. Moreover, CBZ may also come in contact with the top surface nanoparticles of the aggregated  $\text{TiO}_2$  clusters, leaving a large portion of  $\text{TiO}_2$  nanoparticles unused during the photocatalytic process [65]. Additionally, the lesser availability of UV light inside the  $\text{TiO}_2$  clusters may further reduce the efficacy of the photocatalytic process [60].

The effect of recycling on the efficiency and stability of the RGOT composite was investigated by repeating the photocatalytic degradation of CBZ solution for five times, with the results shown in Fig. 10. The RGOT (1:2) optimum combination was selected for the recyclability experiments. It was observed that the RGOT composite could maintain an almost consistent photocatalytic degradation

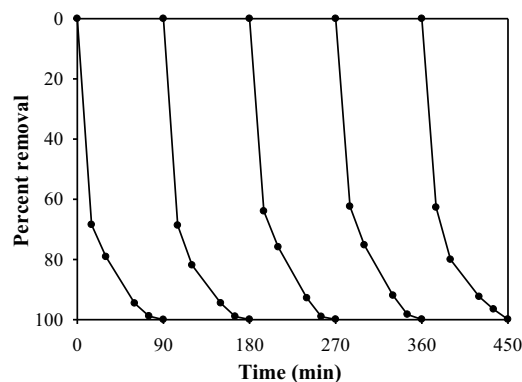


Fig. 10. Cycling runs for the adsorption and photodegradation of CBZ over RGOT aerogel.

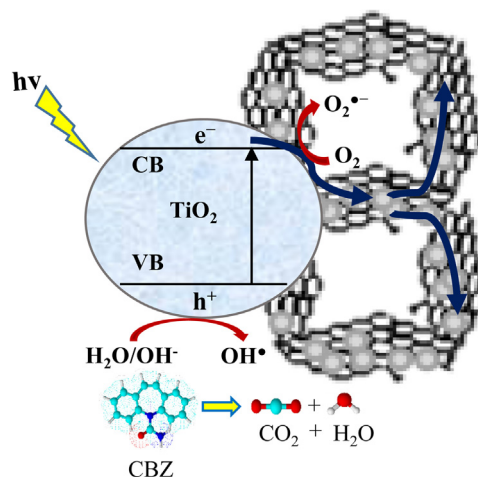


Fig. 11. Schematic diagram of the proposed mechanism of CBZ photodegradation.

ability over five cycles. During all five cycles, the RGOT composite was in contact with the pollutant in such a way that the degraded effluent was seceded and fresh CBZ solution was added while keeping the same concentration. The regenerated photodegradation capability of RGOT may be due to its exposure to UV light, which helped remove the accumulated CBZ from the RGOT surface [61]. This result is in accordance with the study of Zhang et al., where the high adsorption and photocatalytic ability of a  $\text{TiO}_2$ -graphene composite were recovered by exposure to UV light [35].

The photoelectrochemical property of RGOT in the dark and under the illumination of light was studied by using LSV between  $-1.0 \text{ V}$  to  $+1.0 \text{ V}$ . The LSV obtained for RGOT revealed its photosensitivity to light and it can be seen in Fig. S12 that RGOT has higher current under illumination than in the dark which confirms the capability of RGO to collect and transport the photogenerated charges in an effective way. The presence of RGO nanosheets in RGOT increase the electron transfer efficiency and impede the charge recombination in photoexcited  $\text{TiO}_2$  [66] which results in enhanced photocatalytic efficiency of RGOT.

### 3.5. Process mechanism

A probable RGOT photocatalytic mechanism is shown in Fig. 11. UV light excitation of  $\text{TiO}_2$  generates an electron-hole pair (Eq. (5)). The photogenerated electrons move from the valence band (VB) to the conduction band (CB) of  $\text{TiO}_2$  and are then transported to the RGO nanosheets (RGO acts as an electron sink in this case), facilitating oxygen reduction (Eq. (6)). Due to the difference in the work



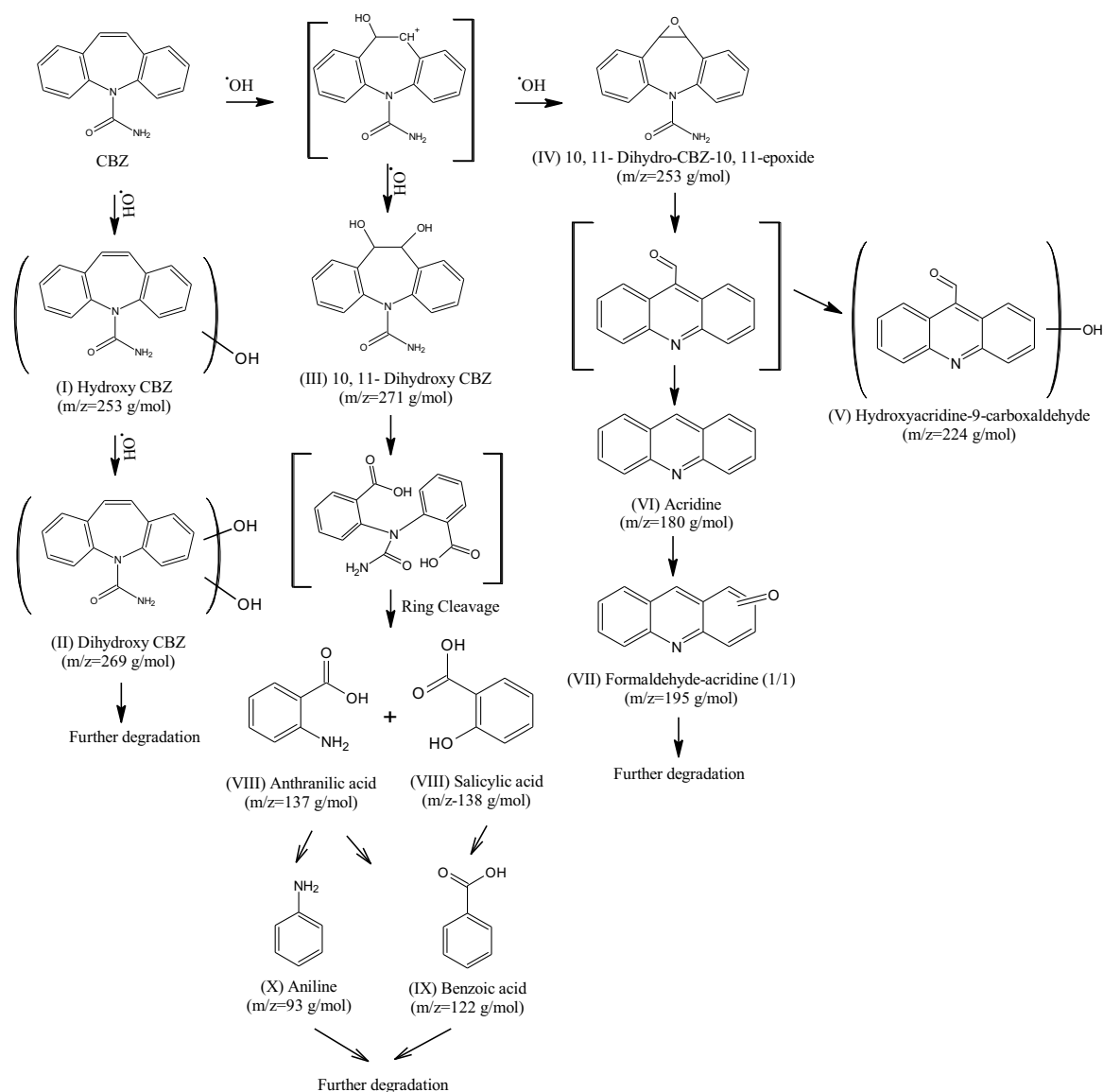
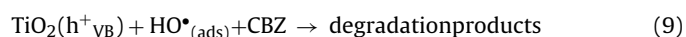
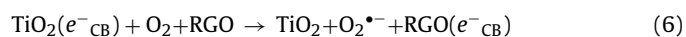


Fig. 12. Degradation pathway and the short-lived and stable intermediates of CBZ photodegradation.

function of RGO ( $-4.42$  eV) and the CB of anatase  $\text{TiO}_2$  ( $-4.4$  eV with a band gap of  $3.2$  eV), the delocalized electrons from the CB reside in the aromatic structure of RGO, suppressing their recombination with VB holes, which results in higher photocatalytic activity [54,67,68]. The 3D structure of the RGOT aerogel may hold the electrons for a longer period of time, since an extended travel path for the electrons is available (Fig. 11) which in turn forms more radical species,  $\text{HO}\cdot$  and  $\text{O}_2^{\cdot-}$ , to promote the degradation of pollutant.



In addition to the inhibited recombination of holes and electrons, the RGO nanosheets can mitigate the mass transfer constraint by increasing the availability of CBZ near the  $\text{TiO}_2$  surface [69]. The low energy state (positive redox potential) of photogenerated holes in the VB also helps to promote the CBZ degradation by either direct

oxidation of CBZ or by generating  $\text{HO}\cdot$  radicals (Eqs. 7 and 8) that later oxidize CBZ (Eq. (9)) [39,64]. Wang et al. reported enhanced degradation due to the interaction of VB holes with the pollutant adsorbed on RGO nanosheets [33]. The effective charge separation achieved by RGO in this study is more or less similar to the effect of incorporated noble metals in the  $\text{TiO}_2$  matrix [17,18], but the enhanced adsorption and the mass transfer of the pollutant near the photocatalyst surface are an additional feature provided by the RGOT aerogel to achieve a high CBZ degradation rate.

### 3.6. Degradation pathway of CBZ

The products of CBZ photodegradation were detected using LC-MS/MS and identified on the basis of their mass spectra. Three commonly detected CBZ transformation products, namely 10,11-dihydro-CBZ-10,11-epoxide, acridine, and anthranilic acid were identified [70,71]. Based on the identified degradation products, a mechanism for CBZ photodegradation was proposed, and the short-lived proposed intermediates (in brackets) were separated from the stable intermediates (in parentheses), with the OH substituents (which could appear at different positions of

the ring) indicated with a line across the parentheses, as shown in Fig. 12. HO• radicals produced during the photocatalytic process attack the CBZ aromatic ring, leading to the formation of intermediate I (monohydroxy CBZ,  $m/z=253$ ). The subsequent addition of another HO• may form intermediate II (dihydroxy CBZ,  $m/z=269$ ). Alternatively, the reaction of short-lived 10-hydroxy-CBZ with HO• can form other degradation products, including intermediate III (10,11-dihydroxy CBZ,  $m/z=271$ ) and the identified intermediate IV (10,11-dihydro-CBZ-10,11-epoxide,  $m/z=253$ ) [72]. Intermediate III is further transformed into another identified product, anthranilic/salicylic acid, by ring cleavage, and intermediates IX (benzoic acid,  $m/z=122$ ) and X (aniline,  $m/z=93$ ) are proposed as further possible degradation products that may be subsequently converted to fully oxidized products, i.e., carbon dioxide (CO<sub>2</sub>) and water (H<sub>2</sub>O). Further degradation of intermediate IV via deamination results in the identified intermediate VI (acridine,  $m/z=180$ ), while intermediates V (hydroxyacridine-9-carboxaldehyde,  $m/z=224$ ) and VII (formaldehyde-acridine (1/1),  $m/z=195$ ) are also probable transformation products [73]. In short, the photocatalytic process can degrade CBZ into different products that may transpire as CO<sub>2</sub> and H<sub>2</sub>O.

#### 4. Conclusions

The *in-situ* and *ex-situ* hydrothermal methods were used to synthesize RGOT hydro-/aerogels, with the RGOT formed only in the latter case owing to the strong interaction between GO and TiO<sub>2</sub> nanoparticles. The anatase form of TiO<sub>2</sub> and the availability of excessive oxygenated functionalities of GO aided RGOT formation. The obtained RGOT exhibited a 3D mesoporous structure, with TiO<sub>2</sub> nanoparticles uniformly anchored onto the RGO sheets. Compared to bare TiO<sub>2</sub>, RGOT showed a synergistic effect up to a certain optimum concentration of TiO<sub>2</sub> in RGOT, RGOT (1:2), which exhibited remarkably high CBZ adsorption and photocatalytic degradation. The chemical coupling of TiO<sub>2</sub> and GO was the key factor for enhanced adsorption and photocatalytic degradation of CBZ, since the CBZ degradation efficiency for the physical mixture of GO and TiO<sub>2</sub> was even lower than for bare TiO<sub>2</sub>. Almost 20% less degradation was observed for lab-made TiO<sub>2</sub> compared to commercial TiO<sub>2</sub>, owing to the aggregation of TiO<sub>2</sub> clusters. The high aggregation degree of the lab-made TiO<sub>2</sub> also resulted in a lesser interaction with GO, possibly accounting for the unsuccessful hydrogel formation in the *in-situ* case. Effective charge separation, enhanced adsorption of CBZ on the RGO sheets, and the mass transfer of CBZ near the photocatalyst surface were additional features provided by the RGOT aerogel compared to other adopted technologies used to increase the quantum yield of TiO<sub>2</sub>, e.g., metal-ion or nonmetal doping, incorporation of noble metals in the TiO<sub>2</sub> matrix, and composites with other metal oxides. Moreover, RGOT was quite efficient in transforming CBZ into products which may finally yield CO<sub>2</sub> and H<sub>2</sub>O in the photocatalytic process. Successful synthesis of the RGOT aerogel and the corresponding high photodegradation of recalcitrant CBZ open up new ways to promote their use to resolve other environmental issues.

#### Acknowledgments

This work was supported by the Human Resource Training Program for Regional Innovation and Creativity through the Ministry of Education (ME) and National Research Foundation (NRF) of Korea (NRF-2014H1C1A1066929). This study was also supported by grants (NRF-2009-0093819, NRF-2016R1A2B4010431) through the ME and NRF of Korea. This research was also supported by an NRF grant from the Korean government (MSIP) (NRF-2015M2A7A1000194).

#### Appendix A. Supplementary data

Supplementary data associated with this article can be found, in the online version, at <http://dx.doi.org/10.1016/j.apcatb.2016.10.007>.

#### References

- [1] W.J. Sim, J.W. Lee, J.E. Oh, Occurrence and fate of pharmaceuticals in wastewater treatment plants and rivers in Korea, *Environ. Pollut.* 158 (2010) 1938–1947.
- [2] Q. Sui, X. Cao, S. Lu, W. Zhao, Z. Qiu, G. Yu, Occurrence, sources and fate of pharmaceuticals and personal care products in the groundwater: a review, *Emerg. Contam.* 1 (2015) 14–24.
- [3] F. Martinez, M.J. Lopez-Munoz, J. Aguado, J.A. Melero, J. Arsuaga, A. Sotto, et al., Coupling membrane separation and photocatalytic oxidation processes for the degradation of pharmaceutical pollutants, *Water Res.* 47 (2013) 5647–5658.
- [4] S.D. Kim, J. Cho, I.S. Kim, B.J. Vanderford, S.A. Snyder, Occurrence and removal of pharmaceuticals and endocrine disruptors in South Korean surface, drinking, and waste waters, *Water Res.* 41 (2007) 1013–1021.
- [5] V.L. Cunningham, C. Perino, V.J. D'Aco, A. Hartmann, R. Bechter, Human health risk assessment of carbamazepine in surface waters of North America and Europe, *Regul. Toxicol. Pharmacol.* 56 (2010) 343–351.
- [6] X.F. Zhou, C.M. Dai, Y.L. Zhang, R.Y. Surampalli, T.C. Zhang, A preliminary study on the occurrence and behavior of carbamazepine (CBZ) in aquatic environment of Yangtze River Delta, China, *Environ. Monit. Assess.* 173 (2011) 45–53.
- [7] A. Bahlmann, W. Brack, R.J. Schneider, M. Krauss, Carbamazepine and its metabolites in wastewater: analytical pitfalls and occurrence in Germany and Portugal, *Water Res.* 57 (2014) 104–114.
- [8] M. Clara, B. Strenn, N. Kreuzinger, Carbamazepine as a possible anthropogenic marker in the aquatic environment: investigations on the behaviour of Carbamazepine in wastewater treatment and during groundwater infiltration, *Water Res.* 38 (2004) 947–954.
- [9] M. Kahle, I.J. Buerge, M.D. Muller, T. Poiger, Hydrophilic anthropogenic markers for quantification of wastewater contamination in ground- and surface waters, *Environ. Toxicol.* 28 (2009) 2528–2536.
- [10] R. Andreozzi, Carbamazepine in water: persistence in the environment, ozonation treatment and preliminary assessment on algal toxicity, *Water Res.* 36 (2002) 2869–2877.
- [11] M. Clara, B. Strenn, O. Gans, E. Martinez, N. Kreuzinger, H. Kroiss, Removal of selected pharmaceuticals, fragrances and endocrine disrupting compounds in a membrane bioreactor and conventional wastewater treatment plants, *Water Res.* 39 (2005) 4797–4807.
- [12] P. Verlicchi, M. Al Aukidy, E. Zambello, Occurrence of pharmaceutical compounds in urban wastewater: removal, mass load and environmental risk after a secondary treatment—a review, *Sci. Total Environ.* 429 (2012) 123–155.
- [13] U.I. Gaya, A.H. Abdullah, Heterogeneous photocatalytic degradation of organic contaminants over titanium dioxide: a review of fundamentals, progress and problems, *J. Photochem. Photobiol. C Photochem. Rev.* 9 (2008) 1–12.
- [14] M.N. Chong, B. Jin, C.W.K. Chow, C. Saint, Recent developments in photocatalytic water treatment technology: a review, *Water Res.* 44 (2010) 2997–3027.
- [15] A. Fujishima, X. Zhang, D.A. Tryk, TiO<sub>2</sub> photocatalysis and related surface phenomena, *Surf. Sci. Rep.* 63 (2008) 515–582.
- [16] S. Kim, S.J. Hwang, W. Choi, Visible light active platinum-ion-doped TiO<sub>2</sub> photocatalyst, *J. Phys. Chem. B* 109 (2005) 24260–24267.
- [17] N. Sobana, M. Muruganadham, M. Swaminathan, Nano-Ag particles doped TiO<sub>2</sub> for efficient photodegradation of direct azo dyes, *J. Mol. Catal. A Chem.* 258 (2006) 124–132.
- [18] P. Fu, P. Zhang, Uniform dispersion of Au nanoparticles on TiO<sub>2</sub> film via electrostatic self-assembly for photocatalytic degradation of bisphenol A, *Appl. Catal. B Environ.* 96 (2010) 176–184.
- [19] M. Dahl, Y. Liu, Y. Yin, Composite titanium dioxide nanomaterials, *Chem. Rev.* 114 (2014) 9853–9889.
- [20] M.S.A. Sher Shah, A.R. Park, K. Zhang, J.H. Park, P.J. Yoo, Green synthesis of biphasic TiO<sub>2</sub>-reduced graphene oxide nanocomposites with highly enhanced photocatalytic activity, *ACS Appl. Mater. Interfaces* 4 (2012) 3893–3901.
- [21] B. Qiu, M. Xing, J. Zhang, Stober-like method to synthesize ultralight porous, stretchable Fe<sub>2</sub>O<sub>3</sub>/graphene aerogels for excellent performance in photo-Fenton reaction and electrochemical capacitors, *J. Mater. Chem. A* 3 (2015) 12820–12827.
- [22] S. Morales-Torres, L.M. Pastrana-Martinez, J.L. Figueiredo, J.L. Faria, A.M.T. Silva, Design of graphene-based TiO<sub>2</sub> photocatalysts—a review, *Environ. Sci. Pollut. Res.* 19 (2012) 3676–3687.
- [23] M.R. Hoffmann, S.T. Martin, W. Choi, D.W. Bahnemann, Environmental applications of semiconductor photocatalysis, *Chem. Rev.* 95 (1995) 69–96.
- [24] R. Leary, A. Westwood, Carbonaceous nanomaterials for the enhancement of TiO<sub>2</sub> photocatalysis, *Carbon* 49 (2011) 741–772.
- [25] A.K. Geim, K.S. Novoselov, The rise of graphene, *Nat. Mater.* 6 (2007) 183–191.
- [26] M.J. Allen, V.C. Tung, R.B. Kaner, Honeycomb carbon: a review of graphene, *Chem. Rev.* 110 (2010) 132–145.

- [27] H. Zhang, X. Lv, Y. Li, Y. Wang, J. Li, P25-graphene composite as a high performance photocatalyst, *ACS Nano* 4 (2009).
- [28] K. Zhou, Y. Zhu, X. Yang, X. Jiang, C. Li, Preparation of graphene-TiO<sub>2</sub> composites with enhanced photocatalytic activity, *New J. Chem.* 35 (2011) 353–359.
- [29] T.D. Nguyen Phan, V.H. Pham, E.W. Shin, H.-D. Pham, S. Kim, J.S. Chung, et al., The role of graphene oxide content on the adsorption-enhanced photocatalysis of titanium dioxide/graphene oxide composites, *Chem. Eng. J.* 170 (2011) 226–232.
- [30] B. Qiu, Y. Deng, M. Du, M. Xing, J. Zhang, Ultradispersed cobalt ferrite nanoparticles assembled in graphene aerogel for continuous photo-fenton reaction and enhanced lithium storage performance, *Sci. Rep.* 6 (2016) 29099.
- [31] F. Sordello, G. Zeb, K. Hu, P. Calza, C. Minero, T. Szkopek, et al., Tuning TiO<sub>2</sub> nanoparticle morphology in graphene-TiO<sub>2</sub> hybrids by graphene surface modification, *Nanoscale* 6 (2014) 6710–6719.
- [32] O.C. Compton, S.T. Nguyen, Graphene oxide, highly reduced graphene oxide, and graphene: versatile building blocks for carbon-based materials, *Small* 6 (2010) 711–723.
- [33] P. Wang, J. Wang, X. Wang, H. Yu, J. Yu, M. Lei, et al., One-step synthesis of easy-recycling TiO<sub>2</sub>-rGO nanocomposite photocatalysts with enhanced photocatalytic activity, *Appl. Catal. B Environ.* 132–133 (2013) 452–459.
- [34] C. Hou, Q. Zhang, Y. Li, H. Wang, P25-graphene hydrogels: room-temperature synthesis and application for removal of methylene blue from aqueous solution, *J. Hazard. Mater.* 205–206 (2012) 229–235.
- [35] Z. Zhang, F. Xiao, Y. Guo, S. Wang, Y. Liu, One-pot self-assembled three-dimensional TiO<sub>2</sub>-graphene hydrogel with improved adsorption capacities and photocatalytic and electrochemical activities, *ACS Appl. Mater. Interfaces* 5 (2013) 2227–2233.
- [36] B. Qiu, M. Xing, J. Zhang, Mesoporous TiO<sub>2</sub> nanocrystals grown in situ on graphene aerogels for high photocatalysis and lithium-ion batteries, *J. Am. Chem. Soc.* 136 (2014) 5852–5855.
- [37] W. Liu, J. Cai, Z. Ding, Z. Li, TiO<sub>2</sub>/RGO composite aerogels with controllable and continuously tunable surface wettability for varied aqueous photocatalysis, *Appl. Catal. B Environ.* 174–175 (2015) 421–426.
- [38] J. William, S. Hummers, R.E. Offeman, Preparation of graphitic oxide, *J. Am. Chem. Soc.* 80 (1958) 1339.
- [39] M. Minella, F. Sordello, C. Minero, Photocatalytic process in TiO<sub>2</sub>/graphene hybrid materials. Evidence of charge separation by electron transfer from reduced graphene oxide to TiO<sub>2</sub>, *Catal. Today* (2016).
- [40] C. Martínez, M. Canle, M.I. Fernández, J.A. Santaballa, J. Faria, Kinetics and mechanism of aqueous degradation of carbamazepine by heterogeneous photocatalysis using nanocrystalline TiO<sub>2</sub>, ZnO and multi-walled carbon nanotubes-anatase composites, *Appl. Catal. B Environ.* 102 (2011) 563–571.
- [41] M. Nawaz, W. Miran, J. Jang, D.S. Lee, Stabilization of Pickering emulsion with surface-modified titanium dioxide for enhanced photocatalytic degradation of Direct Red 80, *Catal. Today* (2016).
- [42] X. Zhang, Z. Sui, B. Xu, S. Yue, Y. Luo, W. Zhan, et al., Mechanically strong and highly conductive graphene aerogel and its use as electrodes for electrochemical power sources, *J. Mater. Chem.* 21 (2011) 6494.
- [43] J.G. Yu, H.G. Yu, B. Cheng, X.J. Zhao, J.C. Yu, W.-K. Ho, The effect of calcination temperature on the surface microstructure and photocatalytic activity of TiO<sub>2</sub> thin films prepared by liquid phase deposition, *J. Phys. Chem. B* 107 (2003) 13871–13879.
- [44] A. Ferrari, J. Robertson, Interpretation of Raman spectra of disordered and amorphous carbon, *Phys. Rev. B* 61 (2000) 14095–14107.
- [45] J. Wang, S.A. Kondrat, Y. Wang, G.L. Brett, C. Giles, J.K. Bartley, et al., Au-Pd nanoparticles dispersed on composite titania/graphene oxide-supports as a highly active oxidation catalyst, *ACS Catal.* 5 (2015) 3575–3587.
- [46] H. Wang, J.T. Robinson, X. Li, H. Dai, Solvothermal reduction of chemically exfoliated graphene sheets, *J. Am. Chem. Soc.* 131 (2009) 9910–9911.
- [47] B. Qiu, Q. Li, B. Shen, M. Xing, J. Zhang, Stöber-like method to synthesize ultradispersed Fe<sub>3</sub>O<sub>4</sub> nanoparticles on graphene with excellent Photo-Fenton reaction and high-performance lithium storage, *Appl. Catal. B Environ.* 183 (2016) 216–223.
- [48] Q. Xiang, J. Yu, M. Jaroniec, Enhanced photocatalytic H<sub>2</sub>-production activity of graphene-modified titania nanosheets, *Nanoscale* 3 (2011) 3670–3678.
- [49] A.A. Ismail, R.A. Geiouhy, H. Bouzid, S.A. Al-Sayari, A. Al-Hajry, D.W. Bahnemann, TiO<sub>2</sub> decoration of graphene layers for highly efficient photocatalyst: impact of calcination at different gas atmosphere on photocatalytic efficiency, *Appl. Catal. B Environ.* 129 (2013) 62–70.
- [50] W.D. Yang, Y.R. Li, Y.C. Lee, Synthesis of r-GO/TiO<sub>2</sub> composites via the UV-assisted photocatalytic reduction of graphene oxide, *Appl. Surf. Sci.* 380 (2015) 249–256.
- [51] F. Wang, K. Zhang, Reduced graphene oxide-TiO<sub>2</sub> nanocomposite with high photocatalytic activity for the degradation of rhodamine B, *J. Mol. Catal. A Chem.* 345 (2011) 101–107.
- [52] B. Song, C. Sizemore, L. Li, X. Huang, Z. Lin, K. Moon, et al., Triethanolamine functionalized graphene-based composites for high performance supercapacitors, *J. Mater. Chem. A* 3 (2015) 21789–21796.
- [53] R. Rahimi, S. Zargari, A. Yousefi, M. Yaghoubi Berijani, A. Ghaffarinejad, A. Morsali, Visible light photocatalytic disinfection of *E. coli* with TiO<sub>2</sub>-graphene nanocomposite sensitized with tetrakis(4-carboxyphenyl)porphyrin, *Appl. Surf. Sci.* 355 (2015) 1098–1106.
- [54] G. Williams, B. Seger, P.V. Kamat, TiO<sub>2</sub>-graphene nanocomposites. UV-assisted photocatalytic reduction of graphene oxide, *ACS Nano* 2 (2008) 1487–1491.
- [55] G. Cheng, M.S. Akhtar, O. Yang, F.J. Stadler, Novel preparation of anatase TiO<sub>2</sub> @ reduced graphene oxide hybrids for high-performance dye-sensitized solar cells, *ACS Appl. Mater. Interfaces* (2013) 6635–6642.
- [56] Y. Li, W. Cui, L. Liu, R. Zong, W. Yao, Y. Liang, et al., Removal of Cr(VI) by 3D TiO<sub>2</sub>-graphene hydrogel via adsorption enriched with photocatalytic reduction, *Appl. Catal. B Environ.* 199 (2016) 412–423.
- [57] M. Nawaz, D. Kim, W. Miran, A. Kadam, J. Heo, S. Shin, et al., Effect of toluene an immiscible pollutant, on the photocatalytic degradation of azo dye, *J. Ind. Eng. Chem.* 30 (2015) 10–13.
- [58] Y. Zhang, Z. Tang, X. Fu, Y. Xu, TiO<sub>2</sub>-graphene nanocomposites for gas-phase photocatalytic degradation of volatile aromatic pollutant: is TiO<sub>2</sub>-graphene truly different from other TiO<sub>2</sub>-carbon composite materials? *ACS Nano* 4 (2010) 7303–7314.
- [59] M. Ziegmann, F.H. Frimmel, Photocatalytic degradation of clofibric acid, carbamazepine and iomeprol using conglomerated TiO<sub>2</sub> and activated carbon in aqueous suspension, *Water Sci. Technol.* 61 (2010) 273–281.
- [60] A. Fujishima, T.N. Rao, D.A. Tryk, Titanium dioxide photocatalysis, *J. Photochem. Photobiol. C Photochem. Rev.* 1 (2000) 1–21.
- [61] S. Linley, Y. Liu, C.J. Ptaček, D.W. Blowes, F.X. Gu, Recyclable graphene oxide-supported titanium dioxide photocatalysts with tunable properties, *ACS Appl. Mater. Interfaces* 6 (2014) 4658–4668.
- [62] F. Zhao, B. Dong, R. Gao, G. Su, W. Liu, L. Shi, A three-dimensional graphene-TiO<sub>2</sub> nanotube nanocomposite with exceptional photocatalytic activity for dye degradation, *Appl. Surf. Sci.* 351 (2015) 303–308.
- [63] D. Wang, X. Li, J. Chen, X. Tao, Enhanced photoelectrocatalytic activity of reduced graphene oxide/TiO<sub>2</sub> composite films for dye degradation, *Chem. Eng. J.* 198–199 (2012) 547–554.
- [64] S. Song, B. Cheng, N. Wu, A. Meng, S. Cao, J. Yu, Structure effect of graphene on the photocatalytic performance of plasmonic Ag/Ag<sub>2</sub>CO<sub>3</sub>-rGO for photocatalytic elimination of pollutants, *Appl. Catal. B Environ.* 181 (2016) 71–78.
- [65] X. Li, J. Yu, M. Jaroniec, Hierarchical photocatalysts, *Chem. Soc. Rev.* 45 (2016) 2603–2636.
- [66] Y.H. Ng, I.V. Lightcap, K. Goodwin, M. Matsumura, P.V. Kamat, To what extent do graphene scaffolds improve the photovoltaic and photocatalytic response of TiO<sub>2</sub> nanostructured films? *J. Phys. Chem. Lett.* 1 (2010) 2222–2227.
- [67] J. Zhang, Z. Xiong, X.S. Zhao, Graphene-metal-oxide composites for the degradation of dyes under visible light irradiation, *J. Mater. Chem.* 21 (2011) 3634.
- [68] W. Wang, J. Yu, Q. Xiang, B. Cheng, Enhanced photocatalytic activity of hierarchical macro/mesoporous TiO<sub>2</sub>-graphene composites for photodegradation of acetone in air, *Appl. Catal. B Environ.* 119–120 (2012) 109–116.
- [69] P. Calza, C. Hadjicostas, V. a. Sakkas, M. Sarro, C. Minero, C. Medana, et al., Photocatalytic transformation of the antipsychotic drug risperidone in aqueous media on reduced graphene oxide-TiO<sub>2</sub> composites, *Appl. Catal. B Environ.* 183 (2016) 96–106.
- [70] N. Tran, P. Drogui, F. Zavisca, S.K. Brar, Sonochemical degradation of the persistent pharmaceutical carbamazepine, *J. Environ. Manag.* 131 (2013) 25–32.
- [71] T.E. Doll, F.H. Frimmel, Removal of selected persistent organic pollutants by heterogeneous photocatalysis in water, *Catal. Today* 101 (2005) 195–202.
- [72] D. Vogna, R. Marotta, R. Andreozzi, A. Napolitano, M. D'Ischia, Kinetic and chemical assessment of the UV/H<sub>2</sub>O<sub>2</sub> treatment of antiepileptic drug carbamazepine, *Chemosphere* 54 (2004) 497–505.
- [73] S. Chiron, C. Minero, D. Vione, Photodegradation processes of the antiepileptic drug carbamazepine, relevant to estuarine waters, *Environ. Sci. Technol.* 40 (2006) 5977–5983.